Link-Level Performance of a Monolithic InP Microwave–Photonic Transceiver for LEO Distributed Radar Crosslinks

Maria Eugenia Serrano F.[a,b], Paolo Ghelfi[b,c], Katarzyna Lawniczuk[a], and Antonella Bogoni[b]

[a]Bright Photonics B.V., 5612AX Eindhoven, The Netherlands
[b]TeCIP Institute, Scuola Superiore Sant'Anna, 56124 Pisa, Italy
[c]National, Inter-University Consortium for Telecommunications (CNIT), 56124 Pisa, Italy

ABSTRACT

Satellite constellations in low Earth orbit (LEO) require inter-satellite communication (ISC) front-ends that meet strict size, weight, and power (SWaP) constraints. Conventional RF front-ends struggle to combine multi-GHz bandwidth, high linearity, and wideband tuning within these budgets. Microwave photonics offers a path forward by using optical components to generate, transport, and process RF signals. However, practical performance can be limited by optical-to-electrical interfaces, packaging, thermal parasitics, etc. This paper motivates a monolithic Indium Phosphide (InP) approach that reduces interconnect loss and minimizes assembly and coupling related performance variations.. As a use-case scenario, we consider a distributed-radar system in which two satellites share waveform generation and reception over an inter-satellite link. We analyze the on-chip transceiver that enables this operation.

This work studies a monolithic Indium Phosphide (InP) microwave–photonic transceiver that co-integrates the transmitter, receiver, and optical amplification on a single chip and quantifies its link-level performance. We perform circuit-level modeling to evaluate gain (G), noise figure (NF), and spurious-free dynamic range (SFDR) across representative C (4–8 GHz), X (8–12 GHz), and Ka (27–40 GHz) bands using realistic device models. The modulator V_π is swept from 2 to 8 V. The results show that the preferred operating region is obtained for low V_π, around 2 to 3 V, and for photodiode input power just below saturation. In this region, the transmitter exhibits representative performance of G$\approx$ +4.5 dB, NF$\approx$ 22.4 dB, and SFDR$\approx$ 110.8 dB·Hz$^{2/3}$, while the receiver exhibits G$\approx$ −8 dB, NF$\approx$ 20 dB, and SFDR$\approx$ 111.2 dB·Hz$^{2/3}$. The results further indicate that the achievable tradeoff among G, NF, and SFDR is bounded by the photodiode linear operating region, and that these metrics must be considered jointly to guide design choices in the monolithic InP transceiver.

Keywords: Microwave photonic radar, photonic integration, indium phosphide, radar transceivers, noise figure, spurious-free dynamic range

1. INTRODUCTION

Emerging space applications increasingly envision satellite constellations not only as communication relays but also as distributed sensing systems. In a distributed or multistatic radar configuration, two or more platforms cooperate to generate, relay, or receive radar waveforms in a phase-coherent manner, enabling functions such as coherent fusion, wider spatial coverage, and potentially improved sensitivity or angular diversity.[1,2] In such architectures, the distribution of stable waveform, timing, and frequency references between nodes becomes a central requirement.

Microwave photonics is attractive for this class of systems because it enables broadband RF signal generation, low phase noise reference transport, and coherent up- and downconversion using optical carriers, while also reducing sensitivity to electromagnetic interference in distribution paths. Thus, the relevance of photonics in this context is not limited to size, weight, and power reduction (SWaP), or very high-frequency operation, but also to coherent signal handling across physically separated radar nodes.[3–5]

Further author information: (Send correspondence to M.E.S.F)
M.E.S.F: E-mail: m.serranoflores@santannapisa.it

Table 1. Comparison of representative PIC-based photonic radar implementations in literature. CL = Conversion Loss; NF = Noise Figure, EOM = Electro-optical modulator, N/R: not reported.

Ref.	Type	Int.	Platform	RF Band	BW	SFDR ($dB{\cdot}Hz^{2/3}$)	NF/CL (dB)	Gain (dB)
[11]	Tx/Rx	No	N/A	up to 40 GHz	200 MHz	N/R	N/R	N/R
[12]	Tx/Rx	Yes	SOI	S	100 MHz	100	NF: 7 dB CL: 55	N/R
[12]	Tx/Rx	Yes	SOI	X	100 MHz	99	CL: 59	N/R
[13]	Tx/Rx	Yes	SOI	X	40 MHz	95	CL: 65	Tx: 40 dB, Rx: 31 dB
[14]	Tx/Rx	Yes	Si	C	2 GHz	101	NF: 54–56	60 dB (LNA)
[14]	Tx/Rx	Yes	Si	Ku	6 GHz	103	NF: 52	60 (LNA)
[15]	Tx/Rx	Yes	Si	Ku	4 GHz	102.7	N/R	57.8
[16]	Tx(EOM) /Rx(EOM)	Yes	TFLN	Ku	10 GHz	102.7	N/R	N/R
[1,2]	Tx/Rx	Yes	SOI + InP	X	N/R	N/R	CL: 54	N/R
This work*	Tx/Rx	Yes	InP	C, X, Ka	N/R	Tx: 110, Rx: 102	NF: Tx: 15, Rx: 17.5	Tx: 10, Rx: -4

* Simulations.

To date, many photonic radar demonstrations have relied on bulk, fiber-based, or hybrid photonic assemblies. While these approaches have successfully demonstrated waveform generation and sensing concepts, they typically require multiple off-chip optical and electrical interfaces, external amplification stages, and packaging-interconnects. These factors increase insertion loss, calibration, and environmental sensitivity, which are especially problematic for compact and repeatable multi-node operation.[6,7]

A monolithic Indium Phosphide (InP) implementation is, therefore, of interest because it can co-integrate active and passive photonic building blocks, including laser sources, semiconductor optical amplifiers, modulators, and photodetectors within a single platform. This makes InP a promising candidate for compact microwave-photonic transceivers intended for coherent inter-satellite radar or crosslink applications.[8,9]

This work investigates the development of a monolithic radar photonic transceiver implemented on an Indium Phosphide (InP) chip for potential LEO inter-satellite applications. The study focuses on system level parameters, conversion gain, noise figure, and spurious-free dynamic range by using circuit-level simulations to quantify the achievable performance in representative C (4–8 GHz), X (8–12 GHz), and Ka (27–40 GHz) scenarios.

2. SYSTEM DESCRIPTION

Several PIC-based microwave–photonic radar systems have been demonstrated, as summarized in Table 1. Most reported implementations are hybrid or only partially integrated, with key functions such as optical amplification, modulation, etc., still realized off chip.[10] Here, we instead study an InP transceiver architecture that integrates the transmitter, receiver, and optical amplification stages on the same photonic chip, enabling tighter co-design of the microwave photonic link and a more compact implementation.

The integrated microwave–photonic link was analyzed using the commercial simulation tool Lumerical INTERCONNECT[17] to evaluate its device level performance across the C-, X-, and Ka-band RF ranges, which are among the most relevant for radar applications.[2] The transceiver is evaluated through circuit-level simulations, with emphasis on conversion gain, noise figure, and spurious-free dynamic range; the fixed device parameters and swept variables are summarized in Table 2.

2.1 Photonic transceiver link analysis

To place the proposed microwave–photonic link in context, Fig. 1 illustrates a possible system-level implementation in which two satellites (P1 and P2) form a distributed radar or inter-satellite communication pair. P1 acts

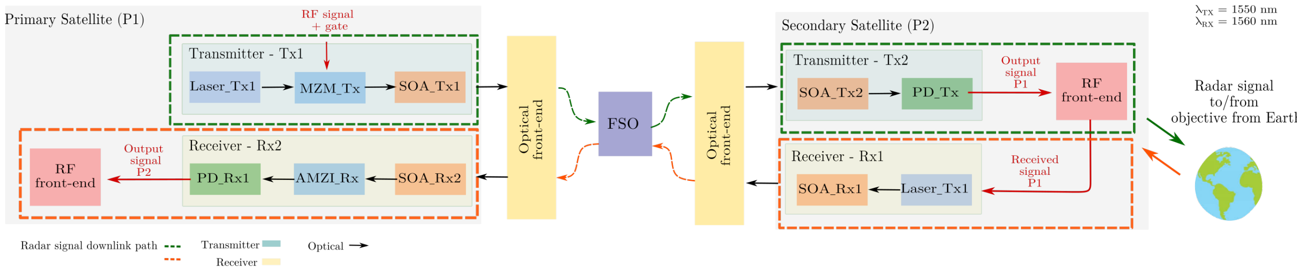

Figure 1. Block-level schematic of the distributed radar system which includes four sub-systems - Tx1, Tx2, Rx1 & Rx2 - realized on a single monolithic InP photonic integrated circuit (PIC) used in simulations. The Tx path includes a CW laser, Mach–Zehnder modulator (MZM) and semiconductor optical amplifier (SOA); the Rx path comprises an optical coupling interface, SOA, coherent or intensity detection stage, and photodiode (PD).

as the primary node, responsible for radar waveform generation, optical modulation, and coherent reception, while P2 operates as the secondary node, hosting the RF front-end and antenna subsystems that interface with the ground segment. This approach allows a radar network composed of one Primary node, feeding multiple secondary nodes. Here we consider a simplified case with only one P2.

The modeled photonic transceiver integrates both transmitter and receiver functions on a single Indium Phosphide (InP) platform, as shown in Fig. 1. The transmitter link at P1 consists of a continuous-wave (CW) laser operating at a wavelength of 1.55 µm, which is applied as an optical carrier to the Mach–Zehnder modulator (MZM_{Tx}), which is driven by a linear-frequency-modulated (LFM) signal at the C-, X-, or Ka-band. A semiconductor optical amplifier (SOA_{Tx1}) compensates for on-chip losses. After amplification, the modulated optical signal is transmitted over a free-space optical (FSO) link to P2.

At the second node P2 (T_{x2}), the signal passes through a second amplification stage (SOA_{Tx2}) and is detected by a high-speed photodiode (PD), which performs optical-to-electrical (O/E) conversion. The converted RF signal is subsequently amplified by the RF front-end and radiated by the antennas toward the Earth.

For the receiver link, the radar echoes collected at P2 are down-converted and filtered in the RF-front end, then used to directly modulate a laser source at 1.56 μm. The detected optical signal is amplified and transmitted back to P1 over the same optical link, where it undergoes a second amplification stage at SOA_{Rx2}. Reflections and leakage from the transmitter laser are rejected using a Mach–Zehnder interferometer with a free spectral range (FSR) of approximately 10 nm, corresponding to a path-length difference of about 65.95 um and a $V_\pi = 3.26\ V$. Finally, a photodiode at P1 performs coherent O/E downconversion to an intermediate frequency (IF), and the resulting signal is passed to the acquisition system for digital processing.

In the present work, the optical segment between nodes is modeled as an equivalent analog photonic transport link. Therefore, the analysis is restricted to the internal gain, noise, and linearity budget of the integrated transceiver and does not yet include explicit free-space optical propagation penalties. These effects will be addressed in future work.

Figure 1 shows the integrated photonic transceiver considered in this work. The circuit-level simulations use realistic component models and loss values summarized in Table 2, based on experimental data and representative InP foundry specifications.

The transceiver performance is evaluated in terms of conversion gain (G_{IF}), noise figure (NF), and spurious-free dynamic range (SFDR), which together describe the efficiency, noise, and linearity of the link. In the simulations, the modulator V_π is swept from 2 to 8 V. It is further assumed that the IF output power is equally split between the photodiode bias network and the 50 Ω load, with a photodiode intermediate frequency output power of 16 dBm.

The noise figure of each section of the link is calculated[18] as,

$$NF = \frac{N_{\text{out}}}{G_{IF} k_B T_0}, \tag{1}$$

Table 2. Fixed device parameters and swept ranges used in the circuit-level simulations.

Parameter	**Value**
Laser output powe	-10 dBm to $+15$
Laser output wavelength	1.55 um
Laser linewidth	1×10^6 Hz
Laser RIN	-157 dBc/Hz
MZM insertion loss	5 dB
MZM extinction ratio	$<$ 20dB
MZM V_π	≤ 2 to 8 V
PD responsivity	0.7 A/W
PD bandwidth	30 GHz
PD saturation	16 dBm
$\mathrm{NF_{SOA}}$	6 dB
Optical amplifier gain	10–15 dB

where k_B is Boltzmann's constant, T_0 is the reference temperature, and N_{out} is the output noise power spectral density, given by

$$N_{\mathrm{out}} = k_B T_0 G_{IF} + k_B T_0 + 2q I_{DC} R_{\mathrm{out}} |H_{PD}|^2 + \mathrm{RIN}\, I_{DC}^2 R_{\mathrm{out}} |H_{PD}|^2. \tag{2}$$

The terms in (2) account for thermal noise, shot noise, and relative intensity noise (RIN) contributions at the link output. The RIN contribution associated with the SOA is related to its noise factor through

$$\mathrm{RIN_{SOA}} = \frac{2h\nu F_0}{P_{\mathrm{in}}}, \tag{3}$$

where P_{in} is the optical power at the amplifier input, and F_0 is the amplifier noise factor.[18]

The simulated G_{IF} and NF results for the C-, X-, and Ka-bands are presented in the following sections as functions of the received optical power at the photodiode, $P_{\mathrm{rx,PD}}$, for V_π values between 2 and 8 V. Here, $P_{\mathrm{rx,PD}}$ is determined by the laser output power and the optical-link gain.

3. RESULTS AND DISCUSSION

Figure 2 collectively shows that the performance of the integrated transceiver is governed by a tradeoff among conversion gain, noise figure, and linearity rather than by a single optimization variable. This can be seen by comparing the transmitter panels in Fig. 2(a)–(c) and the receiver panels in Fig. 2(d)–(f): in both paths, lower V_π improves electro-optic conversion efficiency and, therefore, increases G_{IF}, while higher received optical power at the photodiode improves the link response only up to the edge of the PD linear region. The gain and NF trends are observed in Fig. 2(a), (b), (d), and (e), whereas the corresponding linearity constraint is captured by the SFDR behavior in Fig. 2(c) and (f). Beyond the onset of PD nonlinearity, the benefit of stronger optical beating is offset by distortion and ASE-related noise growth. In the present model, the C-, X-, and Ka-band simulations show nearly identical trends because the analysis isolates the internal microwave–photonic link under common component assumptions.

For the transmitter path, the gain increases as V_π is reduced and as $P_{\mathrm{rx,PD}}$ approaches the maximum value allowed by PD linearity. At $V_\pi = 2$ V, the simulated gain reaches about $+7.37$ dB with NF around 17.45 dB, whereas increasing V_π toward 8 V reduces the gain to about -1 dB and increases the NF to about 25.74 dB. This trend confirms that modulator efficiency is one of the dominant first-order design constraints in the link, since

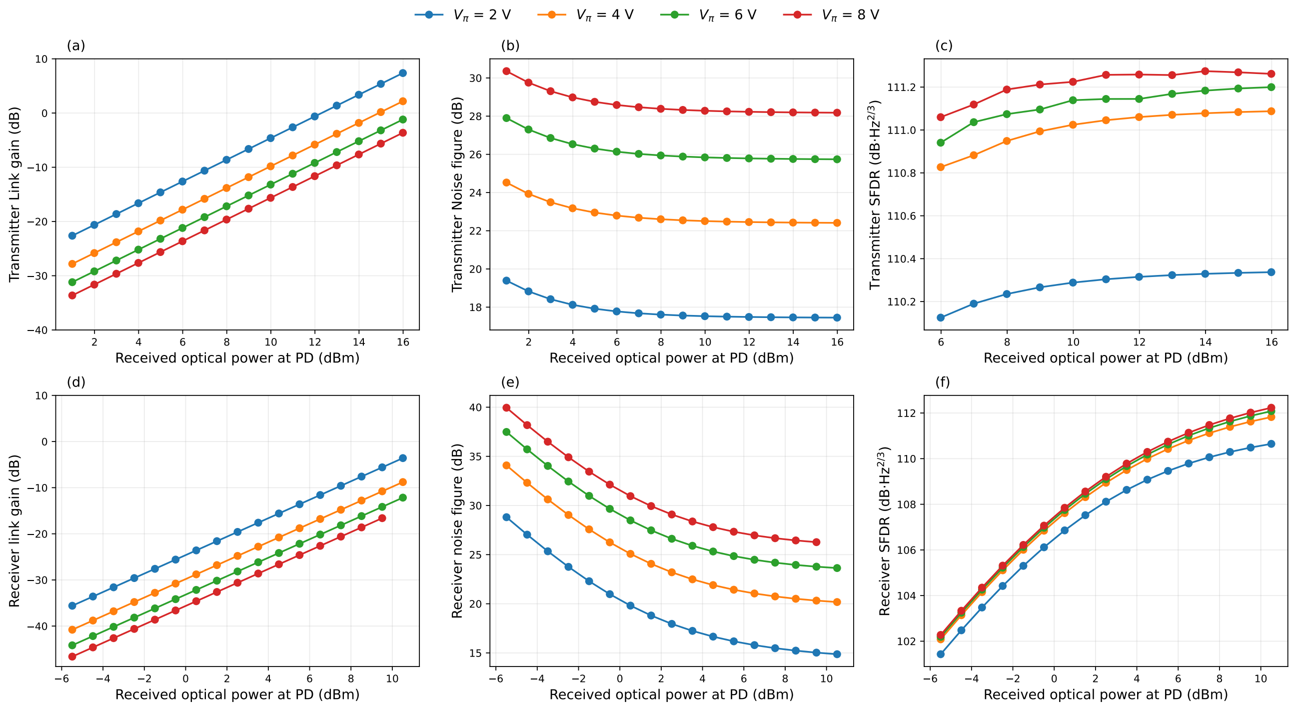

Figure 2. Conversion gain G_{IF}, noise figure (NF), and spurious-free dynamic range (SFDR) as functions of received optical power at the photodiode (PD) for a V_π sweep from 2 to 8 V. Panels (a–c) correspond to the transmitter (Tx) path and show G_{IF}, NF, and SFDR, respectively; panels (d–f) correspond to the receiver (Rx) path and show G_{IF}, NF, and SFDR, respectively. The C-, X-, and Ka-band simulations yielded very similar trends; therefore, only one representative case is presented.

a higher V_π directly increases the required RF drive voltage and reduces the effectiveness of optical-to-electrical conversion. Overall, the best tradeoff is obtained in the low-V_π region, approximately 2 to 3 V in the present sweep, with the $V_\pi = 2$ V case representing the most favorable endpoint.

For the receiver path, the same qualitative dependence is observed, but the link remains more limited regarding loss conversion over the explored operating range compared to the transmitter path. The simulated Rx gain varies from about -3.6 dB down to about -14 dB across the V_π sweep, while the NF spans approximately 15 to 26.13 dB at the operating points selected just below PD saturation. Compared with the Tx case, this indicates that the receiver is more sensitive to accumulated penalties in the and O/E downconversion stages, even when operated near the preferred optical-power region. Accordingly, the Rx path places stricter requirements on the following RF chain. In practical end-to-end implementations, it is expected to benefit from a low-noise RF amplifier after photodetection.

The linearity analysis further clarifies the usable operating range. For the transmitter, SFDR remains relatively flat, around 110 to 111 dB·Hz$^{2/3}$, for $P_{rx,PD}$ values approximately between 0 and +16 dBm, which is below the saturation threshold of the PD. For the receiver, the SFDR spans about 102 to 112 dB·Hz$^{2/3}$ over $P_{rx,PD}$ from roughly -6 to +10 dBm. At higher optical powers, ASE-signal beating and ASE-induced IMD3 products raise the effective noise floor and compress the achievable dynamic range. Therefore, the optimum operating point does not coincide with the highest possible optical power but rather with a bounded region just below PD saturation, where gain is high, NF is low, and SFDR has not yet started to degrade.

Taken together, these results define a practical design window for the monolithic InP transceiver. The preferred regime is obtained by combining the lowest feasible modulator V_π with SOA gain sufficient to push the photodiode close to, but not into compression. In this region, the improvement in conversion efficiency is preserved without incurring excessive saturation related penalties or nonlinear distortion. This observation is important because it transforms the plots of Figure 2 into a co-design, where the SOA gain, modulator efficiency, and PD linearity margin must be selected jointly rather than optimized independently.

From a broader integration perspective, the observed behavior is also consistent with prior analyses of integrated photonic radar links, where conversion loss is dominated by OE/EO efficiency and can be strongly improved by low V_π, higher-power-handling photodiodes, and on-chip optical amplification. The present results, therefore, support the choice of InP as a promising platform since it can combine active optical gain, photodetection, and modulation in a monolithic implementation.

Accordingly, the preferred design target is the highest $P_{rx,PD}$ that remains below the onset of PD compression, combined with the lowest feasible V_π, which would be around 15 dBm and 2 V as a V_π

4. CONCLUSION

This work presented a link-level evaluation of a monolithic InP microwave–photonic transceiver for distributed radar crosslinks and quantified its conversion gain, noise figure, and spurious-free dynamic range as functions of modulator V_π and received optical power at the photodiode. The results show that lower V_π improves electro-optic conversion efficiency and link gain, while increasing optical power improves performance only up to the onset of photodiode nonlinearity. Near saturation, ASE–signal beating and ASE-induced IMD3 increase the effective noise floor and reduce SFDR.

The preferred operating region is obtained just below the photodiode saturation limit, corresponding in the present sweep to approximately $P_{\mathrm{rx,PD}} \approx 15$ dBm and $V_\pi = 2$ V, where gain, NF, and SFDR are jointly optimized. This defines a practical co-design rule in which modulator efficiency, SOA gain, and photodiode linearity margin must be selected together.

These characteristics make the proposed transceiver a promising candidate for distributed radar applications, in which spatially separated nodes must share waveform information and process returned signals coherently. In this context, the ability to combine optical generation, transport, amplification, and detection within the same photonic platform is particularly relevant for maintaining a compact and jointly optimized front-end.

These results also indicate that the photonic link cannot be assessed independently of its electronic interface stages. In particular, practical operation will require analysis of the additional electrical components needed to close the power budget, such as a low-noise amplifier in the receive path before driving the second modulator, as well as intermediate RF gain stages and their associated noise penalties.

A complete system evaluation must therefore include the sensitivity requirements, such as the minimum detectable signal level at the receiver and the electrical drive conditions needed to ensure that the returned signal remains within the usable operating range of the integrated photonic link.

ACKNOWLEDGMENTS

This research was supported by the Horizon Europe project MWP4SPACE, under the Marie Skłodowska-Curie Grant Agreement 101073138 HORIZON-MSCA-2021-DN-01-01

REFERENCES

[1] Camponeschi, F., Gemmato, V., Scotti, F., Porzi, C., Imran, M., Ghelfi, P., Scaffardi, M., and Bogoni, A., "Integrated photonics for enabling coherent radar constellations," in [*2025 25th Anniversary International Conference on Transparent Optical Networks (ICTON)*], 1–4, IEEE (2025).

[2] Reza, M., Maresca, S., Scotti, F., Pandey, G., Imran, M., Serafino, G., Amir, M. H., Camponeschi, F., Ghelfi, P., Bogoni, A., et al., "Multi-static multi-band synthetic aperture radar (sar) constellation based on photonic processing," in [*2022 IEEE International Topical Meeting on Microwave Photonics (MWP)*], 1–4, IEEE (2022).

[3] Marpaung, D., Yao, J., and Capmany, J., "Integrated microwave photonics," *Nature photonics* **13**(2), 80–90 (2019).

[4] Belchovski, M., Benazet, B., Sotom, M., and Rommel, S., "Photonic RF front-end architectures for future satellite payloads," in [*International Conference on Space Optics — ICSO 2024*], **13699**, 2217–2226, SPIE (July 2024).

[5] Zhang, Z., *Millimetre-Resolution Photonics-Assisted Radar*, PhD thesis (2023).

[6] Capmany, J. and Novak, D., "Microwave photonics combines two worlds," *Nature photonics* **1**(6), 319 (2007).

[7] Rinaldi, L., Camponeschi, F., and Bogoni, A., "Space-Grade Analogue and Digital Photonics for Satellite Communications in Europe," *Journal of Lightwave Technology* **42**, 1004–1015 (Feb. 2024). Conference Name: Journal of Lightwave Technology.

[8] Smit, M. M., Williams, K., and Tol, J. V. D., "Past, present, and future of inp-based photonic integration," *APL Photonics* (2019).

[9] Wang, Y., Jiao, Y., and Williams, K. A., "Scaling photonic integrated circuits with inp technology: A perspective," *APL Photonics* (2024).

[10] Pan, S. and Zhang, Y., "Microwave photonic radars," *Journal of Lightwave technology* **38**(19), 5450–5484 (2020).

[11] Ghelfi, P., Laghezza, F., Scotti, F., Serafino, G., Capria, A., Pinna, S., Onori, D., Porzi, C., Scaffardi, M., Malacarne, A., et al., "A fully photonics-based coherent radar system," *Nature* **507**(7492), 341–345 (2014).

[12] Falconi, F., Melo, S., Scotti, F., Malik, M. N., Scaffardi, M., Porzi, C., Ansalone, L., Ghelfi, P., and Bogoni, A., "A combined radar & lidar system based on integrated photonics in silicon-on-insulator," *Journal of Lightwave Technology* **39**(1), 17–23 (2020).

[13] Scotti, F., Porzi, C., Ghelfi, P., Falconi, F., Amir, M. M. H., Maresca, S., Borgarino, M., and Bogoni, A., "Indoor field-trial in x band of a photonics-based multiband radar on a packaged silicon chip," in [*2021 International Topical Meeting on Microwave Photonics (MWP)*], 1–4, IEEE (2021).

[14] Zhong, N., Du, Y., Zou, X., Deng, X., Bai, W., Yang, C., Pan, W., and Yan, L., "Multiple-in-one photonic integrated transceiver for multi-chirp-rate & multi-band isar system and coherent fusion processing," *Journal of Lightwave Technology* (2024).

[15] Li, S., Cui, Z., Ye, X., Feng, J., Yang, Y., He, Z., Cong, R., Zhu, D., Zhang, F., and Pan, S., "Chip-based microwave-photonic radar for high-resolution imaging," *Laser & Photonics Reviews* **14**(10), 1900239 (2020).

[16] Zhu, S., Zhang, Y., Feng, J., Wang, Y., Zhai, K., Feng, H., Pun, E. Y. B., Zhu, N. H., and Wang, C., "Integrated lithium niobate photonic millimetre-wave radar," *Nature Photonics* **19**(2), 204–211 (2025).

[17] ANSYS, Inc., *Ansys Lumerical FDTD: Photonic Integrated Circuit Simulator* (2026). Accessed 2026.

[18] Urick, V. J., Williams, K. J., and McKinney, J. D., [*Fundamentals of microwave photonics*], John Wiley & Sons (2015).